Materials Research Letters

ISSN: 2166-3831 (Online) Journal homepage: www.tandfonline.com/journals/tmrl20

Local composition and nanoindentation response of δ-phase and adjacent γ''-free zone in a Ni-based superalloy

Vitor Vieira Rielli, Felix Theska, Yin Yao, James P. Best & Sophie Primig

To cite this article: Vitor Vieira Rielli, Felix Theska, Yin Yao, James P. Best & Sophie Primig (2022) Local composition and nanoindentation response of δ-phase and adjacent γ' '-free zone in a Ni-based superalloy, Materials Research Letters, 10:5, 301-309, DOI: 10.1080/21663831.2022.2047817

To link to this article: https://doi.org/10.1080/21663831.2022.2047817

© 2022 The Author(s). Published by Informa UK Limited, trading as Taylor & Francis Group

Published online: 10 Mar 2022.

Submit your article to this journal

Article views: 2194

View related articles

View Crossmark data

Citing articles: 7 View citing articles

Full Terms & Conditions of access and use can be found at
https://www.tandfonline.com/action/journalInformation?journalCode=tmrl20

MATER. RES. LETT.
2022, VOL. 10, NO. 5, 301–309
https://doi.org/10.1080/21663831.2022.2047817

ORIGINAL REPORTS

OPEN ACCESS

Local composition and nanoindentation response of δ-phase and adjacent γ''-free zone in a Ni-based superalloy

Vitor Vieira Rielli[a], Felix Theska[a], Yin Yao[b], James P. Best[c,d] and Sophie Primig[a]

[a]School of Materials Science & Engineering, UNSW, Sydney, Australia; [b]Electron Microscopy Unit (EMU), Mark Wainwright Analytical Centre, UNSW, Sydney, Australia; [c]School of Mechanical & Manufacturing Engineering, UNSW, Sydney, Australia; [d]Max-Planck-Institut für Eisenforschung GmbH, Düsseldorf, Germany

ABSTRACT
Experimental differentiation of individual strengthening effects from the nanoscale precipitates in Alloy 718 remains challenging due to co-precipitation of γ' and γ''. Here, we examine a region adjacent to the δ-phase consisting of γ-matrix containing γ'-precipitates only. The width and compositional profile of this γ''-free zone is uncovered via high-resolution characterization. Nanomechanical analyses reveal that the lack of γ''-precipitates lower the hardness of the γ''-free zone by 10–20%, while the δ-phase is found to be $\sim$80% harder than the γ-matrix. These findings may guide mechanical modelling and microstructural engineering of stronger superalloys critical to aerospace industry.

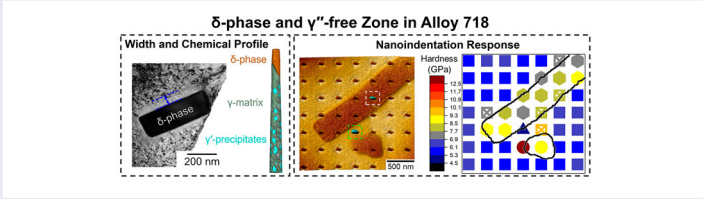

IMPACT STATEMENT
First experimental evidence of hardness reduction in γ''-free zone close to the δ-phase boundary, highlighting the strengthening effect of γ''-precipitates. Previously unknown mechanical properties of the δ-phase are reported.

ARTICLE HISTORY
Received 28 January 2022

KEYWORDS
Superalloy; δ-phase; precipitates; γ''-free zone; nanoindentation

1. Introduction

Ni-based superalloys containing γ'' (Ni_3Nb, $D0_{22}$) and γ' ($Ni_3(Al,Ti)$, $L1_2$) precipitates such as Alloy 718 are known for their excellent mechanical properties up to 650°C [1]. The impact of these nanoscale phases on strengthening has been a recurring subject of investigation [2–5]. Particle-dislocation relationship theories on order and coherency strengthening are generally accepted to describe precipitation effects in Ni-based superalloys [6,7]. In Alloy 718, coherency strengthening dominates over order strengthening due to the relatively high γ/γ'' lattice misfit [3]. This is affected by the size, volume fraction, and configuration of the precipitates [8,9]. Experimental measurements to determine specific γ' and γ'' contributions to strength remain challenging and scarcely explored. Elevated temperatures above 700°C cause coarsening of γ''-precipitates and transformation into the stable, platelet-shaped δ-phase (Ni_3Nb, $D0_a$) [10], or direct precipitation of δ-phase on grain boundaries [9]. Low volume fractions of δ-phase are beneficial to grain size control and fatigue properties, while high fractions may deteriorate the high-temperature strength [11]. In the proximity of the δ-phase, γ''-free zones are commonly observed and underpin the competition for Nb between these two phases [10,12,13]. However, despite numerous micromechanical studies on Alloy 718 [14–16], the local composition and impact on the mechanical properties of the δ-phase and γ''-free zone remain unclear. The absence of γ''-precipitates has the potential to deteriorate mechanical strength, heightening stress localization at grain boundaries with δ-phase precipitates. As consequence, accelerated intergranular crack growth [17,18] and potential early fracture of critical

CONTACT Sophie Primig s.primig@unsw.edu.au School of Materials Science & Engineering, UNSW, Sydney, NSW 2052, Australia

© 2022 The Author(s). Published by Informa UK Limited, trading as Taylor & Francis Group
This is an Open Access article distributed under the terms of the Creative Commons Attribution-NonCommercial License (http://creativecommons.org/licenses/by-nc/4.0/), which permits unrestricted non-commercial use, distribution, and reproduction in any medium, provided the original work is properly cited.

aerospace components make the investigation of the local mechanical response and chemical compositions of the γ''-free zone crucial.

The present study explores the previously unknown local composition, microstructure, and mechanical properties of the δ-phase and adjacent γ''-free zone in Alloy 718. Transmission electron microscopy (TEM) and atom probe microscopy (APM) reveal that the γ''-free zone contains γ'-precipitates only. This is the result of a (Al + Ti)/Nb concentration gradient from the δ-phase into the γ-matrix. The local mechanical response of the γ-matrix, the γ''-free zone, and δ-phase is studied with nanoindentation within a scanning electron microscope (SEM) and atomic force microscopy (AFM). The findings indicate the magnitude of mechanical property variation over the microstructure and allow a more accurate description of the mechanical behaviour of Alloy 718 on the local scale. Modelling efforts to design aerospace parts with better high temperature properties may benefit from the current findings.

2. Materials and methods

Samples from forged and directly aged Alloy 718 turbine disk were provided by voestalpine BÖHLER Aerospace GmbH & Co KG, Austria. TEM specimens were ground to 50 μm thickness and electrolytically polished using a STRUERS A2 electrolyte. TEM bright-field micrographs were recorded with a JEOL 2100 at 200 kV acceleration voltage. FIJI ImageJ was used to determine the width of the γ''-free zone from six δ-phase platelets [19].

APM samples were prepared via standard techniques [20]. A Cameca LEAP 3000 atom probe was used in voltage acquisition mode. Parameters were as follows: 50 K temperature, 20% pulse fraction, 200 kHz pulse frequency, and 1.0% evaporation rate. Data analysis was done using the Cameca AP Suite 6.1, and the reconstruction was calibrated using atom probe crystallography protocols [21]. Concentration profiles were extracted with a step size of 25 nm.

For the nanoindentation experiments, samples were polished to 1 μm diamond solution followed by colloidal silica suspension. Identification markers around selected δ-phase regions were created with focused ion beam milling in a FEI Nova Nanolab 200. To avoid artifact generation, the sample surface was not exposed to the ion beam for imaging. A commercial *in situ* nanoindentation system (Alemnis ASA, Alemnis AG, Switzerland) with a conductive-diamond cube corner indenter tip (Synton-MDP, Switzerland) was installed into a FEI Nova NanoSEM 230. Nanoindentation testing was performed under load control with target maximum load of 225 μN, corresponding to an indentation depth of 60–100 nm. Indents were performed in a 9 × 8 grid, with ~ 600 nm spacing between indents. *In situ* measurements with the cube corner probe allowed for direct observation of the tip apex and local microstructure during testing, so that site-specific measurements could be made over the region of interest.

For AFM nanoindentation testing, a diamond NM-RC-C (Bruker) probe was installed on a Bruker Dimension ICON to generate a 14 × 14 grid of indents 300 nm apart. Testing was performed with 80 V ramp size and 2 V ramp setpoint, corresponding to a load of 34 μN. A TiN coated Si wafer was used to calibrate the deflection sensitivity, while the spring constant of the AFM cantilever was determined Sader method [22]. After indentation measurements were completed, a SCANASYST-AIR tip (Bruker) was used to scan the surface via peak-force tapping mode. The NanoScope Analysis 1.7 software was used to process the AFM images and determine the residual contact area of the indents. Hardness was estimated from the maximum load determined experimentally, and the contact area of the residual indents measured by AFM [23,24].

3. Results and discussion

3.1. Microstructure and chemistry of δ-phase and γ''-free zone

Figure 1(a) provides a TEM micrograph representing the γ-matrix close to the δ-phase. No precipitates are identified in the δ-phase proximity as highlighted in blue. Densely arranged, nanoscale γ'/γ'' co-precipitates are found in the γ-matrix as highlighted in red and Figure 1(b). γ' and γ'' precipitates can be identified in bright-field micrographs due to their surrounding strain fields [25]. The co-precipitate morphology of duplets and triplets in Alloy 718 is commonly observed [8,26]. Thus, the γ''-free zone of the δ-phase must contain either no precipitates or precipitates with insufficient lattice mismatch to appear in the bright field micrograph. This appears similar to observations in ALLVAC® 718Plus or Alloy 718 variants, where this has been referred to as precipitate-free or depletion zones [27–29]. In the present work, the magnitude of such a zone has been measured as highlighted in Figure 1(a, c), with a width of 72 ± 7 nm. This is smaller than reported in previous studies [27–29], but an exact comparison is difficult as the exact dimensions may depend on the alloy composition, thermo-mechanical history, and/or location of the δ-phase on grain boundaries. In the present study, δ-phase particles are commonly encountered along grain boundaries, so that the accelerated diffusivity of solutes may affect the observed γ''-free zone [30]. An overview analysis of

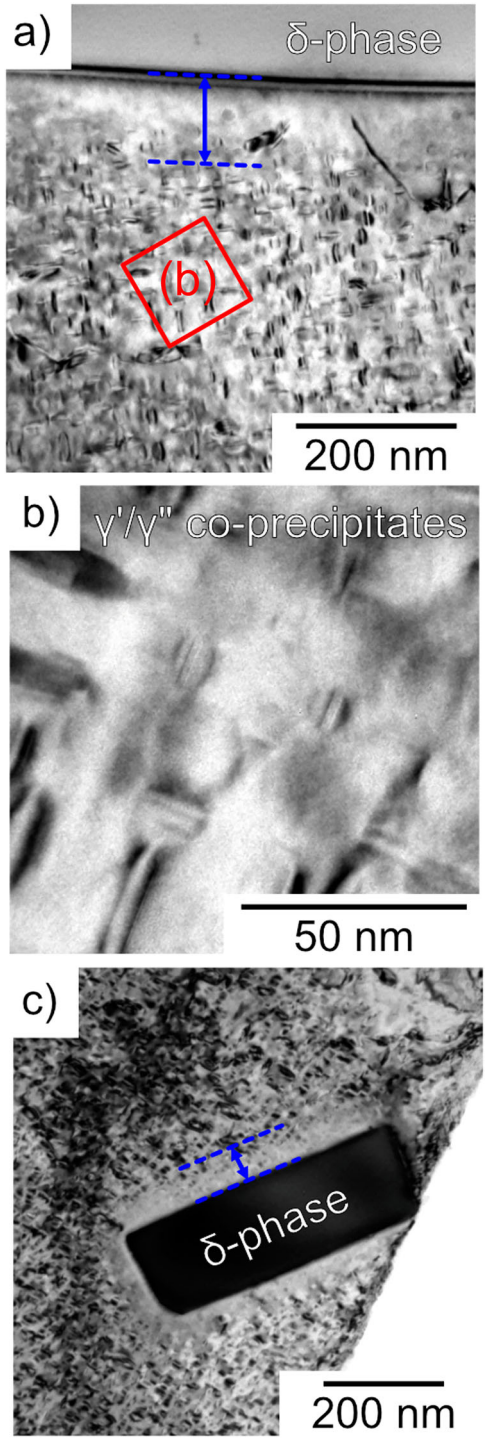

Figure 1. (a) The γ-matrix near the δ-phase appears precipitate-free. Blue dimensions represent the extend and red highlights a region within the γ-matrix. (b) Within the γ-matrix, γ'/γ'' co-precipitates are densely arranged. (c) Blue represents the extend measured of the γ''-free zone around the γ-matrix.

the microstructure of similarly manufactured materials is provided in [31].

The APM reconstruction in Figure 2(a) confirms that the designated γ''-free zone is indeed free of the γ''-phase and contains only nanoscale γ'-precipitates. The tip orientation, however, is likely at a low angle to the δ-phase, since the γ''-free zone extends to ~ 250 nm from the phase boundary, larger than the γ''-free zone measured perpendicularly with TEM. Local Al and Ti segregation in the γ-matrix is observed, whereas Nb and Ti segregate into the δ-phase [32,33]. Up to 9 at.% of Nb is also commonly observed in γ'-precipitates [8]. No obvious inhomogeneities are found in the Ni map. The Nb concentration in γ''-precipitates may be as high as 20 at.% [8], however, the Nb iso-concentration surfaces do not show γ''-precipitates close to the δ-phase, indicating that the existing precipitates in the volume are solely γ'-precipitates. Nb-rich regions indicating the presence of γ''-precipitates, partially captured in the APM volume, are mostly found towards the thick end of this dataset (red arrows) away from the δ-phase. The volume fraction of 18.4% of γ'-precipitates (turquoise) is in line with previous reports [9]. The diameter of these precipitates ranges from 0.8 to 16.3 nm, although a limited number of γ'-precipitates were fully captured within the APM dataset. The (Al + Ti)/Nb ratio is plotted for γ'-precipitates and γ-matrix (green) in Figure 2(b). Inside γ'-precipitates, this ratio drops moderately with increasing distance from the δ-phase. This trend is more pronounced in the γ-matrix, which exhibits a sharp drop. In Alloy 718, the (Al + Ti)/Nb ratio strongly influences the precipitation of γ' and γ''. Cozar & Pineau [34] demonstrated that increasing this ratio in the bulk concentration favours a 'compact morphology', dominated by γ'-precipitates. Detor et al. [35] used this approach to stabilize γ'-precipitates against coarsening in Alloy 718 variants. The (Al + Ti)/Nb ratio also influences co-precipitate formation on a local scale [26]. Increasing the (Al + Ti)/Nb ratio promotes γ' precipitation, whereas decreasing the (Al + Ti)/Nb ratio is in favour of γ'' [26,35]. Thus, as the (Al + Ti)/Nb ratio increases in proximity of the δ-phase, γ'' precipitation is suppressed and γ' precipitation favoured. Changes in the local chemistry likely originate from the δ-phase capturing Nb. This observation correlates well with the TEM micrographs shown in Figure 1. Reportedly, γ'-precipitates exhibit a lower lattice mismatch to the γ-matrix, and thus, will be less visible in TEM bright field micrographs [36].

3.2. Nanoscale mechanical probing of δ-phase and γ''-free zone

In situ nanoindentation within the SEM was used to place cube corner indentations over a local region of interest containing δ-phase particles. The backscatter electron micrograph in Figure 3(a) shows that most indents were placed on the γ-matrix, while a smaller number

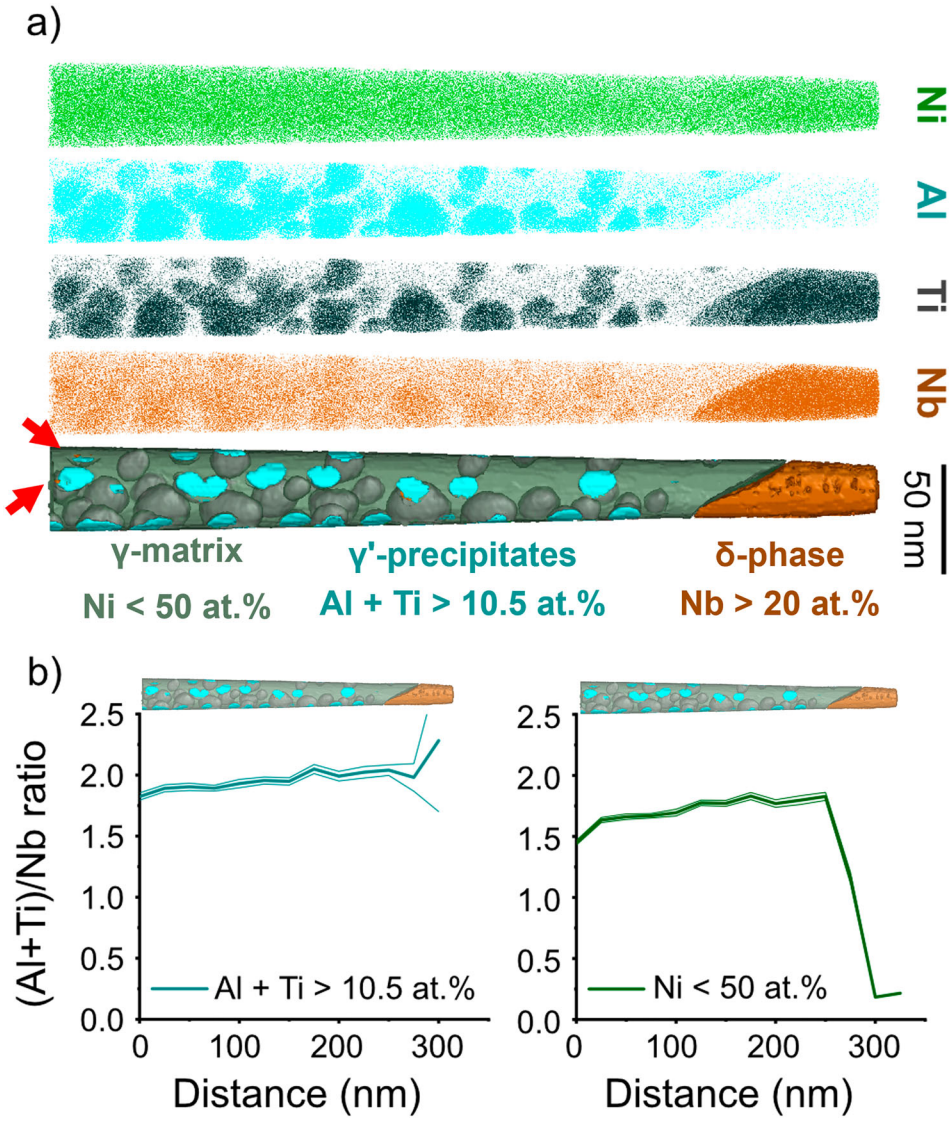

Figure 2. (a) Ni, Al, Ti and Nb atom maps in side-view reveal pronounced segregation of Al and Ti into γ'-precipitates. Segregation of Nb in the δ-phase is obvious, but less clear for smaller precipitates. The iso-concentration surfaces reveal the presence of γ'-precipitates and the absence of γ''-precipitates close to the δ-phase. (b) Plots of the (Al + Ti)/Nb ratio within γ' (turquoise) and the γ-matrix (green), with standard deviation. In γ'-precipitates, the ratio falls gently with the distance from the δ-phase. This trend is clearer within the γ-matrix, and also exhibits a sharp drop away from the δ-phase.

hit δ-phase particles and their surrounding areas. The region within the red dashed box was studied in greater depth. As exemplified in the highlighted impressions in the 3D AFM image in Figure 3(b), the residual contact area was determined individually for each indent. Values of $\sim 5 \times 10^4\,\mathrm{nm}^2$ on the γ-matrix (green box) and $\sim 2.6 \times 10^4\,\mathrm{nm}^2$ on the δ-phase (white box) are highlighted in the figure. Indents on the δ-phase particles are consistently shallower and of lower contact area than those of the γ-matrix. The representative load vs displacement curves in Figure 3(c) show steeper loading and consequent lower displacement until maximum load is reached at a depth of 70 nm on the δ-phase, in comparison to 95 nm on the γ-matrix. The unloading profile can be correlated to the elastic recovery of the indent, where the shaded areas below the unloading curves show that the elastic energy of the δ-phase for a $\sim 225\,\mu\mathrm{N}$ indent is twice as large as the γ-matrix, with values of 1.8 and 0.9 pJ, respectively. For all indents, pile-up formation is expected as the ratio between residual indentation depth (measured via AFM) and maximum indentation depth (obtained from load vs displacement curves) is > 0.7 [37]. This is confirmed via AFM topology imaging (Figure 3(b)).

The hardness map in Figure 3(d) shows that the hardness of the γ-matrix varies from 4 to 6.1 GPa, with an average value of 5.0 ± 0.4 GPa (■), which is in alignment with what has been reported in literature [16,38].

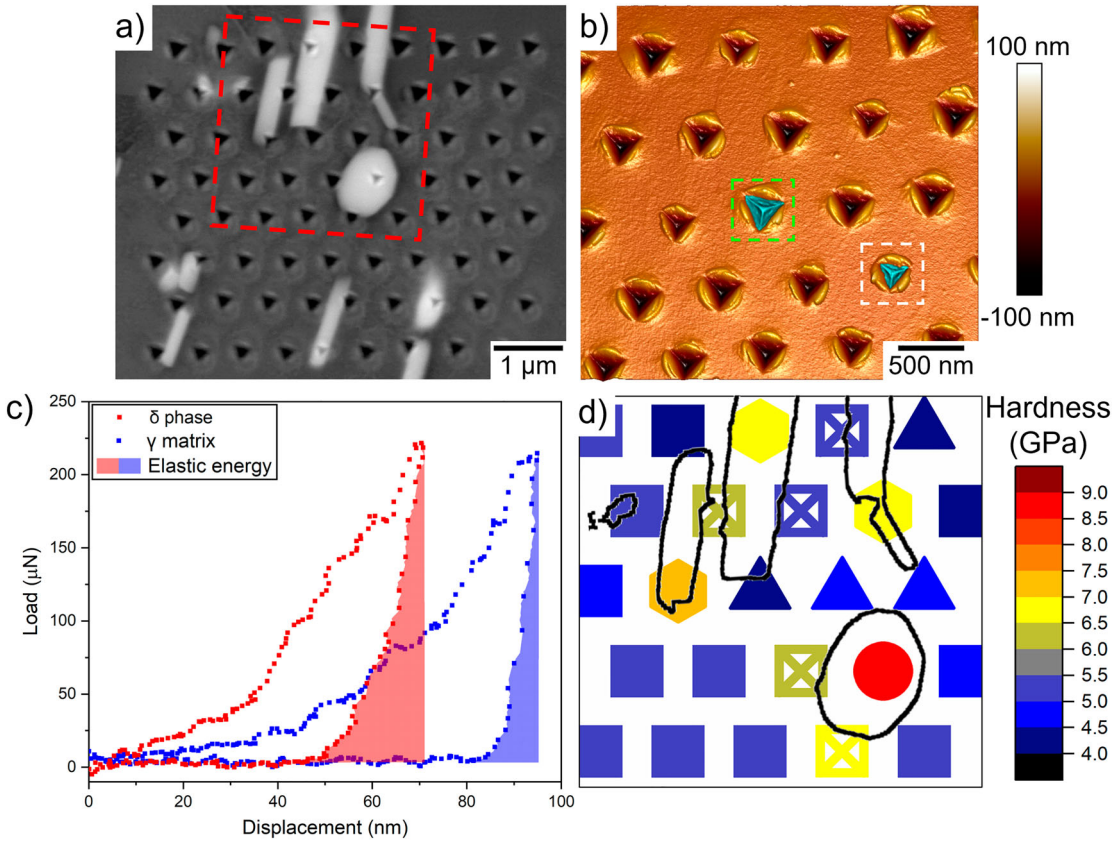

Figure 3. (a) Nanoindentation grid around multiple δ-phase particles (b) 3D AFM image of red dashed region shown in (a). Selected impressions on the γ-matrix and δ-phase enclosed by green and white dashed boxes, respectively, show the residual contact area highlighted in turquoise. (c) Representative load vs displacement plot of nanoindentations on the δ-phase and on the γ-matrix in (b), where shaded areas highlight the elastic energy. (d) Hardness map of indents within red dashed box in (a). The δ-phase particles are indicated by black lines. The markers indicate round δ-phase (●), platelet δ-phase (■), γ-matrix (■), γ''-free zone (▲), and the squared markers with an X show indents not used in the calculation of the γ-matrix hardness.

As the δ-phase is commonly found at grain boundaries, the observed scatter in hardness may be caused by indentation of multiple grains in the γ-matrix with different crystallographic orientations [39]. However, the proximity of the δ-phase seems to be a more critical factor, as a 4.5 ± 0.4 GPa hardness is observed in a likely γ''-free zone (▲). Other indents close to δ-phase particles exhibit hardness of 5.9 ± 0.7 GPa (squared markers with an X). These indents might have been affected either by the surrounding hard δ-phase particles, striking them underneath the surface, minimizing the softening effect of the γ''-free zone, or by dislocation pile-up at phase boundaries. Consistent with the observation of greater elastic energy at the same load, Figure 3(d) shows that δ-phase is also up to 76% harder than the γ-matrix with maximum value of 8.8 GPa estimated for the round particle (●). For the platelet shaped particles, hardness is 7.1 ± 0.3 GPa (■). This variation in hardness between platelet and round particles is likely an effect of the δ-phase orientation, where the harder, round particle seems to be a cross section of a rod. Therefore, larger volume of δ-phase underneath the indent makes it more representative of the actual material response. However, precise quantification from these indents is unrealistic due to uncertainties from overlapping plastic zones, material pile up, and difficulties in determining exact contact areas [40–42].

The indents in Figure 3 are much larger than the γ''-free zone (Figure 1), and additionally made at the lower-end of the system load-limit (0.5 N load cell). Therefore, further experimentation by AFM nanoindentation was carried out as shown in Figure 4, as improved spatial resolution can be achieved through the controlled application of lower loads (~ 34 μN). The grid of indents around two δ-phase particles is displayed in Figure 4(a). The 3D AFM image of the red dashed box is shown in Figure 4(b). Similar to Figure 3, a platelet and a round δ-phase are found, and as demonstrated in Figure 4(c), the highest estimated hardness is also seen on the round particle. Compared to Figure 3(d), hardness values are higher in general, reaching up 10.9 ± 2.4 GPa for the round δ-phase (●), 8.1 ± 0.5 GPa for the platelet (■) and 6.0 ± 0.3 GPa

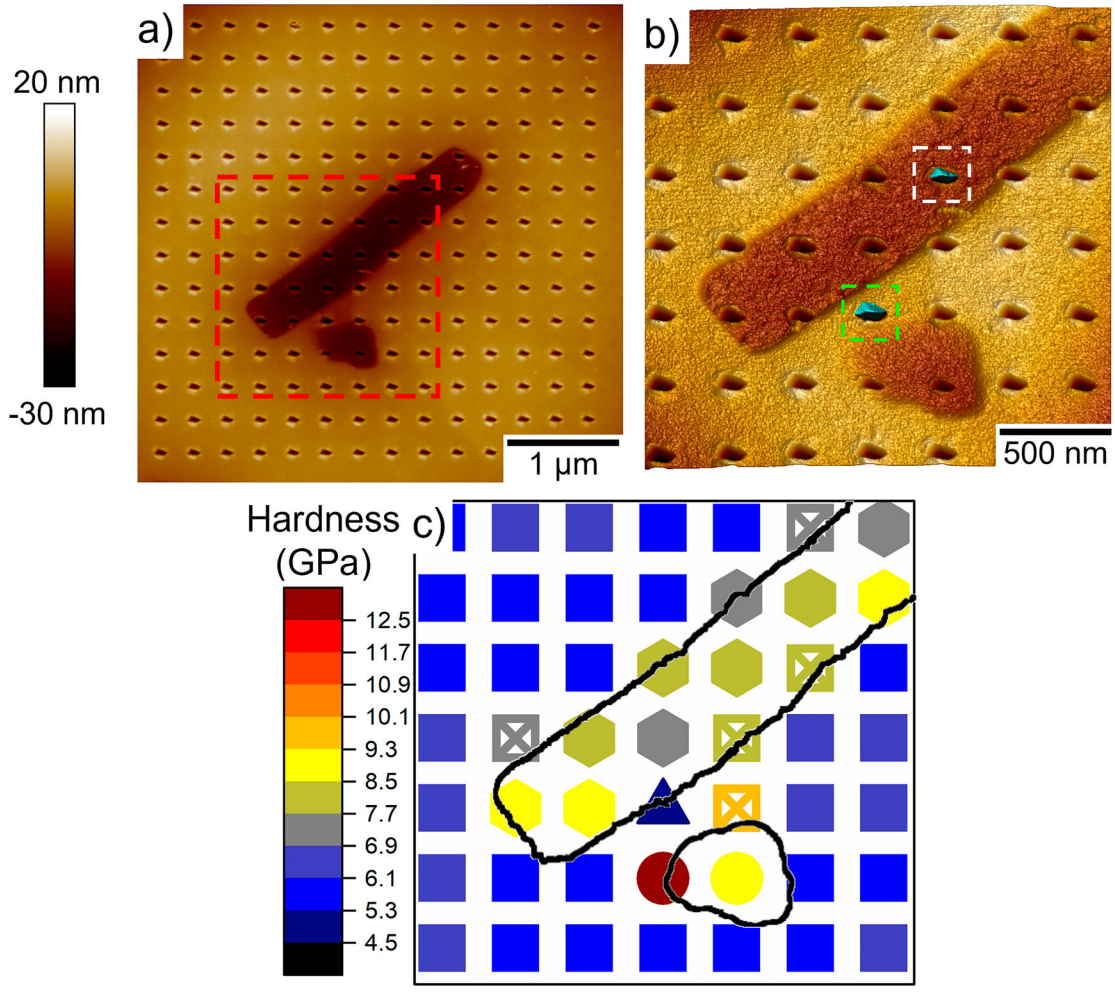

Figure 4. (a) AFM tomography image of a nanoindentation grid produced using AFM around δ-phase particles. (b) 3D AFM image of red dashed region shown in (a). Selected impressions on the γ-matrix and δ-phase enclosed by white dashed boxes show residual contact area highlighted in turquoise. (c) Hardness map of indents within red dashed box in (a). The δ-phase particles are outlined by black lines. The markers indicate round δ-phase (●), platelet δ-phase (■), γ-matrix (■), γ''-free zone (▲), and the squared markers with an X show indents not used in the calculation of the γ-matrix hardness.

for the γ-matrix (■). This might be a consequence of the indentation size effect, where hardness is a function of the depth of the impression, and shallower indents lead to higher measured hardness for the same materials [43,44]. Topography effects additionally observed for the δ-phase, which is ca. 10 nm sunken into the surface, are likely chemo-mechanical artefacts induced during polishing. The stepped surface height difference at the γ-matrix/δ-phase interface may lead to inaccuracies for proper interpretation of hardness on interphase regions, where indents that fall directly on this interface as identified by squared markers with an X in Figure 4(c). Hardness values in these areas are higher than in γ-matrix regions far from the δ-phase, as residual indents are slanted and distorted, and measured contact areas smaller. However, one indent highlighted in the green box in Figure 4(b) is located between round and platelet δ-phases which is likely a γ''-free zone (▲); for this indent a 20% lower hardness of 4.8 GPa compared to the remaining γ-matrix was found. A Welch's unequal variances t-test at $\alpha = 0.05$ rejected the null hypothesis regarding this datapoint as part of the remaining γ-matrix data-set, therefore, it can be categorized as statistically significantly different from the γ-matrix. It should also be noted that the shallower indents (on average 18 ± 2 nm) carried out with AFM generate a much smaller plastic zone size and an ideal spacing of 15–20x the indentation depth corresponds to $\sim$270 to 360 nm apart, which correlates well to the used spacing of 300 nm.

Nanomechanical testing as used in this study is highly complex considering all variables regarding indenter geometry, errors in contact area due to pile-up formation, and interactions between the material and indenter at such low loads [40–42]. Thus, mixed quantitative and qualitative interpretation of similar findings is generally considered. However, nanoindentation techniques as the

Table 1. Nanoindentation hardness analysis from both nanoindenter and AFM measurements.

Feature	Marker	Hardness nanoindenter (GPa)/(*N*)	% Change	Hardness AFM (GPa)/(*N*)	% Change
γ-Matrix	■	5.0 ± 0.4 (13)	–	6.0 ± 0.3 (32)	–
δ-Phase platelet	■	7.1 ± 0.3 (3)	42	8.1 ± 0.5 (10)	35
δ-Phase round	•	8.8 (1)	76	10.9 ± 2.4 (2)	82
γ''-Free zone	▲	4.5 ± 0.4 (4)	−10	4.8 (1)	−20

Provided are % change values in reference to the γ-matrix, and indent number (N).

ones employed here, and posterior analysis of the residual contact area have been shown to provide good estimations of hardness [45,46]. In particular, nanoindentation using AFM allows for reasonable results at very high spatial resolution [47]. The general findings presented here related to the lower hardness values on the γ''-free zone, corroborate that γ'-precipitates provide lower contribution to hardness due to their ordering strengthening. Here we show that the lack of γ''-precipitates cause a decrease in local hardness of 10–20% compared to the γ-matrix. As the volume fraction and diameter of γ'-precipitates in Figure 2 is similar to regions of γ-matrix away from the γ''-free zone [9] and due to their limited strengthening effect [5], the absence of the γ''-precipitates plays a much larger role in the hardness decrease than the morphological aspects of the γ'-precipitates. However, the γ''-precipitates account for 37–51% of the strength of Alloy 718 [5], therefore, the hardness in the γ''-free zone is higher than expected. When indenting within the γ''-free zone, the plastic zone radiating from the indent is not necessarily fully confined within this region. Interaction of the plastic zone with either the harder δ-phase interface (submerged or otherwise), or γ''-precipitates at the zone boundary, would generate an increased hardness compared to the γ''-free material. Additionally, the samples were directly aged after forging, consequently, limited dislocation annihilation occurred. The presence of a dislocation rich network on areas adjacent to the δ-phase [48] might also induce a work hardening response during indentation, generating hardness higher than expected. Table 1 summarizes mechanical properties obtained via nanoindentation. These findings on the previously unknown harder behaviour of the δ-phase, and softer adjacent γ''-free zone, further advance mechanical studies on these important secondary phases in Ni-based superalloys.

4. Conclusion

This study uncovers the microstructural, chemical, and nanomechanical features of the δ-phase and its surrounding γ''-free zone in Alloy 718 via correlative characterization techniques. Increased (Al + Ti)/Nb ratio maintains γ' precipitation and supresses γ'' precipitation in a 72 ± 7 nm zone around the δ-phase. The mechanical response of the γ''-free zones and the δ-phase particles are investigated via nanoindentation experiments, enabling the individual impact of γ' and γ'' on hardness to be experimentally determined. The absence of γ''-precipitates is observed to reduce the γ-matrix hardness by up to 20%, while the round cross-section δ-phase is $\sim$80% harder than γ-matrix. These finding improve our understanding about the local mechanical behaviour in Alloy 718 enabling better computational modelling and further alloy engineering of stronger superalloys.

Acknowledgements

The authors thank Drs. Takanori Sato and Hongwei Liu at the Australian Centre for Microscopy and Microanalysis at the University of Sydney, and Dr. Simon Hager at the Electron Microscopy Unit at Mark Wainwright Analytical Centre at UNSW and acknowledge access to these facilities via Microscopy Australia. The authors thank voestalpine BÖHLER Aerospace GmbH & Co KG (Austria) for providing the materials and Bernd Oberwinkler, Aleksandar Stanojevic, Christian Gruber, and Flora Godor for scientific discussions.

Disclosure statement

No potential conflict of interest was reported by the author(s).

Funding

This work was supported by the Australian Research Council Linkage Projects [grant numbers LP180100144, LP190101169] and UNSW Scientia Fellowship scheme.

References

[1] Reed RC. The superalloys: fundamentals and applications. London: Cambridge University Press; 2008.
[2] Oblak JM, Paulonis DF, Duvall DS. Coherency strengthening in Ni base alloys hardened by DO22 γ' precipitates. Metall Trans. 1974;5:143–153.
[3] Chaturvedi MC, Han YF. Strengthening mechanisms in Inconel 718 superalloy. Met Sci. 1983;17:145–149.
[4] Zhang S, Lin X, Wang L, et al. Strengthening mechanisms in selective laser-melted Inconel718 superalloy. Mater Sci Eng A [Internet]. 2021;812:141145. DOI:10.1016/j.msea.2021.141145.
[5] Rielli VV, Godor F, Gruber C, et al. Effects of processing heterogeneities on the micro- to nanostructure strengthening mechanisms of an alloy 718 turbine disk. Mater Des [Internet]. 2021;212:110295. https://www.sciencedirect.com/science/article/pii/S0264127521008509.

[6] Goodfellow AJ. Strengthening mechanisms in polycrystalline nickel-based superalloys. Mater Sci Technol [Internet]. 2018;34:1793–1808. DOI:10.1080/02670836.2018.1461594.
[7] Ardell AJ. Precipitation hardening. Metall Trans A. 1985;16:2131–2165.
[8] Rielli VV, Theska F, Godor F, et al. Evolution of nanoscale precipitates during common Alloy 718 ageing treatments. Mater Des [Internet]. 2021;205:109762. DOI:10.1016/j.matdes.2021.109762.
[9] Theska F, Stanojevic A, Oberwinkler B, et al. On conventional versus direct ageing of Alloy 718. Acta Mater [Internet]. 2018;156:116–124. DOI:10.1016/j.actamat.2018.06.034.
[10] Kirman I, Warrington DH. The precipitation of Ni3Nb phases in a Ni-Fe-Cr-Nb alloy. Metall Trans. 1970;1:2667–2675.
[11] Anderson M, Thielin AL, Bridier F, et al. Δ phase precipitation in Inconel 718 and associated mechanical properties. Mater Sci Eng A [Internet]. 2017;679:48–55. DOI:10.1016/j.msea.2016.09.114.
[12] Rielli VV, Theska F, Primig S. Correlative approach for atom probe sample preparation of interfaces using plasma focused ion beam without lift-out. Microsc Microanal. 2021;27:1–11.
[13] Sundararaman M, Mukhopadhyay P, Banerjee S. Precipitation of the δ-Ni3Nb phase in two nickel base superalloys. Metall Trans A. 1988;19:453–465.
[14] Sawant A, Tin S, Zhao JC. High temperature nanoindentation of ni-base superalloys. Proc Int Symp Superalloys. 2008: 863–871.
[15] Munther M, Palma T, Tavangarian F, et al. Nanomechanical properties of additively and traditionally manufactured nickel-chromium-based superalloys through instrumented nanoindentation. Manuf Lett [Internet]. 2020;23:39–43. https://www.sciencedirect.com/science/article/pii/S2213846319300902.
[16] Orozco-Caballero A, Gutierrez C, Gan B, et al. High-throughput nanoindentation mapping of cast IN718 nickel-based superalloys: influence of the Nb concentration. J Mater Res [Internet]. 2021;36:2213–2222. DOI:10.1557/s43578-021-00133-5.
[17] Rezende MC, Araújo LS, Gabriel SB, et al. Oxidation assisted intergranular cracking under loading at dynamic strain aging temperatures in Inconel 718 superalloy. J Alloys Compd [Internet]. 2015;643:S256–S259. https://www.sciencedirect.com/science/article/pii/S0925838815007847.
[18] Ghonem H, Nicholas T, Pineau A. Elevated temperature fatigue crack growth in alloy 718—part I: effects of mechanical variables. Fatigue Fract Eng Mater Struct. 1993;16:565–576.
[19] Schindelin J, Arganda-Carreras I, Frise E, et al. Fiji: an open-source platform for biological-image analysis. Nat Methods. 2012;9:676–682.
[20] Gault B, Moody MP, Cairney JM, et al. Atom probe microscopy. New York: Springer Science & Business Media; 2012.
[21] Gault B, Moody MP, Cairney JM, et al. Atom probe crystallography. Mater Today [Internet]. 2012;15:378–386. DOI:10.1016/S1369-7021(12)70164-5.
[22] Sader JE, Chon JWM, Mulvaney P. Calibration of rectangular atomic force microscope cantilevers. Rev Sci Instrum. 1999;70:3967–3969.
[23] Doerner MF, Nix WD. A method for interpreting the data from depth-sensing indentation instruments. J Mater Res [Internet]. 1986;1:601–609. https://www.cambridge.org/core/article/method-for-interpreting-the-data-from-depthsensing-indentation-instruments/F15B242DEAD2C9CE6B42E9CCA31D522C.
[24] Oliver WC, Pharr GM. An improved technique for determining hardness and elastic madulus using load and displacement. J Mater Res. 1992;7:1564–1583.
[25] Carter BA, Williams DB, Carter CB, et al. Transmission electron microscopy: a textbook for materials science. Diffraction. II. Boston (MA): Springer Science & Business Media; 1996.
[26] Theska F, Nomoto K, Godor F, et al. On the early stages of precipitation during direct ageing of Alloy 718. Acta Mater [Internet]. 2020;188:492–503. DOI:10.1016/j.actamat.2020.02.034.
[27] Deleume J, Cloué JM, Andrieu E. Influence of δ phase precipitation on the stress corrosion cracking resistance of alloy 718 in PWR primary water. J Nucl Mater [Internet]. 2008;382:70–75. DOI:10.1016/j.jnucmat.2008.09.018.
[28] Sharma J, Nicolaÿ A, De Graef M, et al. Phase discrimination between δ and η phases in the new nickel-based superalloy VDM Alloy 780 using EBSD. Mater Charact [Internet]. 2021;176:111105. https://www.sciencedirect.com/science/article/pii/S1044580321002357.
[29] Viskari L, Cao Y, Norell M, et al. Grain boundary microstructure and fatigue crack growth in Allvac 718Plus superalloy. Mater Sci Eng A [Internet]. 2011;528:2570–2580. https://www.sciencedirect.com/science/article/pii/S0921509310013675.
[30] Flewitt PEJ, Wild RK. Grain boundaries: Their microstructure and chemistry. 2001.
[31] Theska F, Stanojevic A, Oberwinkler B, et al. Microstructure-property relationships in directly aged Alloy 718 turbine disks. Mater Sci Eng A [Internet]. 2020;776:138967. DOI:10.1016/j.msea.2020.138967.
[32] Viskari L, Stiller K. Atom probe tomography of Ni-base superalloys Allvac 718Plus and Alloy 718. Ultramicroscopy [Internet]. 2011;111:652–658. DOI:10.1016/j.ultramic.2011.01.015.
[33] Páramo-Kañetas PJ, Ozturk U, Calvo J, et al. Analysis of strain-induced precipitates by delta-processing in Inconel 718 superalloy. Mater Charact [Internet]. 2021;173:110926. https://www.sciencedirect.com/science/article/pii/S1044580321000565.
[34] Cozar R, Pineau A. Morphology of y'and y" precipitates and thermal stability of inconel 718 type alloys. Metall Trans. 1973;4:47–59.
[35] Detor AJ, DiDomizio R, Sharghi-Moshtaghin R, et al. Enabling large superalloy parts using compact coprecipitation of γ' and γ''. Metall Mater Trans A Phys Metall Mater Sci. 2018;49:708–717.
[36] McAllister D, Lv D, Deutchman H, et al. Characterization and modeling of deformation mechanisms in Ni-base superalloy 718. Proc Int Symp Superalloys. 2016: 821–829.
[37] Bolshakov A, Pharr GM. Influences of pileup on the measurement of mechanical properties by load and depth

sensing indentation techniques. J Mater Res [Internet]. 1998;13:1049–1058. https://www.cambridge.org/core/article/influences-of-pileup-on-the-measurement-of-mechanical-properties-by-load-and-depth-sensing-indentation-techniques/CB4A16D9AFCAE75CAEA01E38B435E1B5.

[38] Wang H, Dhiman A, Ostergaard HE, et al. Nanoindentation based properties of Inconel 718 at elevated temperatures: a comparison of conventional versus additively manufactured samples. Int J Plast [Internet]. 2019;120:380–394. DOI:10.1016/j.ijplas.2019.04.018.

[39] Ju S-P, Wang C-T, Chien C-H, et al. The nanoindentation responses of nickel surfaces with different crystal orientations. Mol Simul [Internet]. 2007;33:905–917. DOI:10.1080/08927020701392954.

[40] Guillonneau G, Wheeler JM, Wehrs J, et al. Determination of the true projected contact area by in situ indentation testing. J Mater Res. 2019;34:2859–2868.

[41] Oliver WC, Pharr GM. Measurement of hardness and elastic modulus by instrumented indentation: advances in understanding and refinements to methodology. J Mater Res. 2004;19:3–20.

[42] Strader JH, Shim S, Bei H, et al. An experimental evaluation of the constant β relating the contact stiffness to the contact area in nanoindentation. Philos Mag. 2006;86:5285–5298.

[43] Milman YV, Golubenko A.A., Dub SN. Indentation size effect in nanohardness. Acta Mater [Internet]. 2011;59:7480–7487. https://www.sciencedirect.com/science/article/pii/S1359645411006021.

[44] Almasri AH, Voyiadjis GZ. Nano-indentation in FCC metals: experimental study. Acta Mech. 2010;209:1–9.

[45] Miyake K, Fujisawa S, Korenaga A, et al. The effect of pile-up and contact area on hardness test by nanoindentation. Japanese J Appl Phys. 2004;43:4602–4605.

[46] Li Z, Cheng YT, Yang HT, et al. On two indentation hardness definitions. Surf Coat Technol. 2002;154:124–130.

[47] Neumeier S, Pyczak F, Göken M. Influence of rhenium and ruthenium on the local mechanical properties of the γ and γ' phases in nickel-base superalloys. Philos Mag. 2011;91:6435.

[48] Wang Y, Zhen L, Shao WZ, et al. Hot working characteristics and dynamic recrystallization of delta-processed superalloy 718. J Alloys Compd [Internet]. 2009;474:341–346. https://www.sciencedirect.com/science/article/pii/S0925838808010542.